CrossMark

Structural characterization and luminescence properties of bluish-green-emitting SrCaMgSi$_2$O$_7$:Eu^{2+}, Dy^{3+} phosphor by solid-state reaction method

Ishwar Prasad Sahu · D. P. Bisen ·
Nameeta Brahme · Lata Wanjari ·
Raunak Kumar Tamrakar

Abstract An excellent long afterglow SrCaMgSi$_2$O$_7$:Eu^{2+}, Dy^{3+} phosphor was prepared by the high-temperature solid-state reaction method. The phase structure of prepared phosphor was an akermanite-type structure, which belongs to the tetragonal crystallography with space group P$\bar{4}2_1$m. Chemical composition of the sintered SrCaMgSi$_2$O$_7$:Eu^{2+}, Dy^{3+} phosphor was confirmed by EDX. Under ultraviolet excitation, the SrCaMgSi$_2$O$_7$:Eu^{2+}, Dy^{3+} phosphor would emit bluish-green (cyan) light, belonging to the broad emission band ascribed to the $4f^6 5d^1 \rightarrow 4f^7$ transition. Investigation of afterglow properties show that SrCaMgSi$_2$O$_7$:Eu^{2+}, Dy^{3+} phosphor held a fast and slow decay process. The peak of ML intensity increases linearly with increasing impact velocity of the moving piston. The CIE chromaticity diagram and ML spectra show a similar spectrum as PL spectra, which indicated that ML is emitted from the same emitting center of Eu^{2+} ions. Thus the present investigation indicates that the piezoelectrically induced de-trapping model is responsible to produce ML in prepared SrCaMgSi$_2$O$_7$:Eu^{2+}, Dy^{3+} phosphor.

Keywords SrCaMgSi$_2$O$_7$:Eu^{2+}, Dy^{3+} · Photoluminescence · Long afterglow · Mechanoluminescence

I. P. Sahu (✉) · D. P. Bisen · N. Brahme · L. Wanjari
School of Studies in Physics and Astrophysics, Pt. Ravishankar Shukla University, Raipur 492010, India
e-mail: ishwarprasad1986@gmail.com

R. K. Tamrakar
Department of Applied Physics, Bhilai Institute of Technology (Seth Balkrishan Memorial), Durg 491001, India

Introduction

Photoluminescent material with long afterglow is a kind of energy-storage material that can absorb both ultraviolet (UV) and visible light from sunlight and gradually release the energy in the darkness at a certain wavelength. This kind of long afterglow material has been widely studied by many researchers since ancient times [1–4]. In 2000, a new kind of long afterglow phosphors based on the silicate was synthesized by Xiao et al. [5]. The new materials include alkaline earth magnesium disilicates doped with Eu^{2+} and trivalent rare earth ions, $M_2MgSi_2O_7:Eu^{2+}$, R^{3+} (M = Ca, Sr, Ba; R = Nd, Dy, Tm). These phosphors have characteristics of bright intensity, heat stability, chemical and physical stability, low cost, and especially an excellent water-resistant property [6–8].

Luminescence induced during any mechanical action on materials is known as mechanoluminescence (ML). ML can be excited by grinding, rubbing, cutting, cleaving, shaking, scratching, crushing, compressing, or by impulsive deformation of solids. It can also be excited by thermal shocks caused by drastic cooling or heating of materials or by the shockwaves produced during exposure of samples to laser pulses or ultrasonic waves. ML also appears during the deformation caused by the phase transition or growth of certain crystals as well as during separation of two solids in contact. ML has been observed in insulators, semiconductors, as well as in conductors [9]. ML has found various important applications such as impact sensors in spacecrafts (the emission intensity can be used to determine the kinetic energy of impact), fracture sensor, damage sensor, stress sensor for the visualizations of stress field near the crack-tip, stress distribution in solids, and quasi-dynamic crack propagation in solids, etc. Thus, many researchers have focused on the investigation of phosphors with high ML [10]. Until now, some phosphors with high ML, such as red phosphors $BaTiO_3$–$CaTiO_3$:Pr, [11] green phosphors $SrAl_2O_4$:Eu, [12, 13] yellow phosphors ZnS:Mn, [14] and blue phosphor $CaYAl_3O_7$:Eu etc., [15] have been developed. However, the requirement of application for ML sensors is still not satisfied with the development of ML materials. At the same time, the high stabilities, such as resistance of water, thermal stability, are also very important for the application of ML. More ML phosphors with strong ML intensity and high stability are needed.

It is well known that silicates have a higher physical and chemical stability after water treatment. Furthermore, Eu^{2+}-doped and Dy^{3+} co-doped silicates phosphors display various colors of light. Therefore, in this paper, we investigate the structural characterization and luminescence properties of Eu^{2+}-doped and Dy^{3+} co-doped strontium calcium magnesium disilicates ($SrCaMgSi_2O_7:Eu^{2+}$, Dy^{3+}) phosphor by the high-temperature solid-state reaction method. The phase structure, crystallite size, surface morphology, elemental analysis, and different stretching modes were analyzed by X-ray diffractometer (XRD), transmission electron microscopy (TEM), field emission scanning electron microscopy (FESEM) with energy-dispersive X-ray spectroscopy (EDX), and fourier transform infrared (FTIR) spectra, respectively. Luminescence properties were also investigated on the basis of photoluminescence (PL), long afterglow (decay), ML and ML spectra.

Experimental

Phosphor preparation

The Eu^{2+}-doped and Dy^{3+} co-doped strontium calcium magnesium disilicates namely $SrCaMgSi_2O_7$:Eu^{2+}, Dy^{3+} phosphor was prepared by the high-temperature solid-state reaction method. The raw materials are strontium carbonate [$SrCO_3$ (99.90 %)], calcium carbonate [$CaCO_3$ (99.90 %)], magnesium oxide [MgO (99.90 %)], silicon di-oxide [SiO_2 (99.99 %)], europium oxide [Eu_2O_3 (99.99 %)], and dysprosium oxide [Dy_2O_3 (99.99 %)], all of analytical grade (A.R.), were employed in this experiment. Boric acid (H_3BO_3) was added as flux. Initially, the raw materials were weighed according to the nominal compositions of $SrCaMgSi_2O_7$:Eu^{2+}, Dy^{3+} phosphor, and then the powders were mixed and milled thoroughly for 2 h using agate mortar and pestle. The ground sample was placed in an alumina crucible and subsequently fired at 1,300 °C for 3 h in a weak reducing atmosphere. The weak reducing atmospheres were generated with the help of activated charcoal. At last, the nominal compounds were obtained after the cooling down of a programmable furnace. The work of reducing atmosphere is to convert Eu^{3+} to Eu^{2+} ions. In order to investigate the phase structure of the $SrCaMgSi_2O_7$: Eu^{2+}, Dy^{3+} phosphor, we also prepare $Sr_2MgSi_2O_7$: Eu^{2+}, Dy^{3+} and $Ca_2MgSi_2O_7$: Eu^{2+}, Dy^{3+} phosphors at same temperature. Solid-state reaction method is widely used to prepare silicate-based phosphors because samples prepared using this method has good luminescence and very good morphology.

Characterization techniques

The phase structures of the prepared $SrCaMgSi_2O_7$:Eu^{2+}, Dy^{3+} phosphor were characterized by powder X-ray diffraction analysis (XRD). Powder XRD pattern was obtained from Bruker D8 advanced X-ray powder diffractometer using Cu-Kα radiation and the data were collected over the 2θ range of 10–80°. The phase structure of the sample was verified with the help of Joint Committee of Powder Diffraction Standard Data (JCPDS) file (JCPDS: 75-1736, JCPDS 87-0046). Particle size of prepared phosphor was determined by TEM using TECHNAI G2 by FEI. The samples required for TEM analysis were prepared by dispersing the $SrCaMgSi_2O_7$:Eu^{2+}, Dy^{3+} phosphor in methanol using an ultrasound bath technique. A drop of this dispersed suspension was put onto a 200-mesh carbon-coated copper grid and then dried in the air. The morphological images of prepared phosphor were collected by the FESEM. The samples were coated with a thin layer of gold (Au) and then the surface morphology of prepared phosphor was observed by a field emission scanning electron microscope (FESEM; ZIESS Ulta Plus-55) operated at the acceleration voltage of 5 kV. EDX was used for the elemental (qualitative and quantitative) analysis of the prepared phosphor. FTIR spectra were recorded in the middle infrared region ($4,000$–$400 cm^{-1}$) with the help of IR Prestige-21 by SHIMADZU. For investigating the functional groups ($4,000$–$1,400 cm^{-1}$) and fingerprint region ($1,400$–$400 cm^{-1}$) of FTIR spectra, potassium bromide (KBr, A.R. grade) were mixed with prepared $SrCaMgSi_2O_7$:Eu^{2+}, Dy^{3+} phosphor. The excitation and emission spectra were

recorded on a spectrofluorophotometer, Shimadzu (RF 5301-PC) using a spectral slit width of 1.5 nm. The long afterglow (decay) curves were obtained using a Perkin Elmer fluorescent spectrometer with the proper excitation under a UV lamp (365 nm). The ML measurement was observed by the home made lab system comprising of an RCA-931A photomultiplier tube (PMT). The ML glow curve can be plotted with the help of SM-340 application software installed in a computer attached with the storage oscilloscope and ML spectrum was recorded with the help of different band pass interference (400–700 nm) filter. All measurements were carried out at room temperature.

Experimental setup for mechanoluminescence (ML) measurement

The experimental set up used for the impulsive deformation of ML was shown in Fig. 1. A load of particular mass and shape was dropped from different heights for striking the prepared $SrCaMgSi_2O_7:Eu^{2+}$, Dy^{3+} phosphor at different impact velocities. In this experiment, the mass of the dropping load was 400 g and the shape of the load was cylindrical. The phosphor under study was placed on the upper surface of a transparent Lucite plate and it was then covered with a thin aluminum foil and fixed with adhesive tape. The foil reflects light and prevents scattering of the fragments during the impact of a moving piston onto the prepared phosphor. This arrangement eliminates the error in the ML measurement due to the scattering of the crystallite fragments during the impact of the load onto the phosphor. The housing is made up of thick soft iron to provide shielding from light and magnetic field. The slit
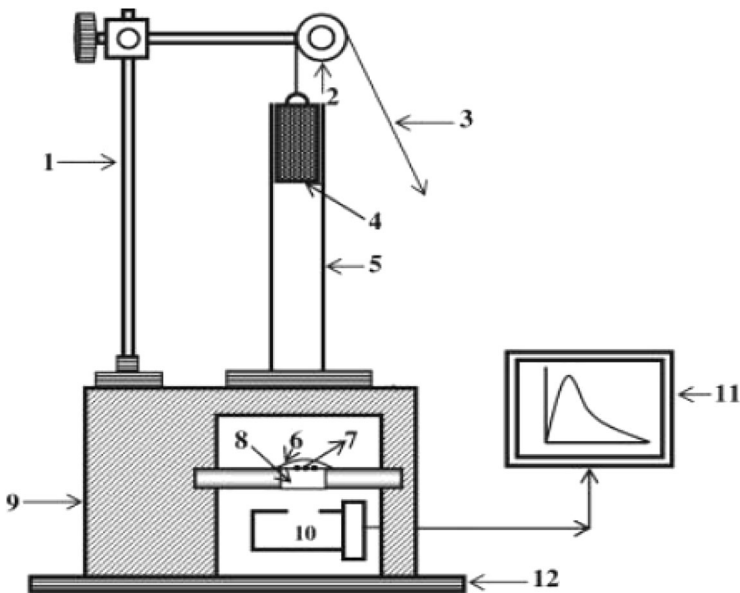

Fig. 1 Schematic diagram of the experimental setup for ML measurement. *1* Stand, *2* pulley, *3* metallic wire, *4* load, *5* guiding cylinder, *6* aluminium foil, *7* phosphor, *8* transparent Lucite plate, *9* wooden block, *10* photomultiplier tube (PMT), *11* storage oscilloscope, *12* iron base mounted on a table

arrangement at the window is provided to adjust the size of the window according to the incident beam. When the phosphor placed on the Lucite plate was crushed by impact of the load, light is emitted.

By changing the distance between the piston to be dropped and the sample placed on the Lucite plate, the impact velocity (v_0) of the load could be changed, since the pulley and the guiding cylinder used were of negligible friction, the impact velocity (v_0) was taken as $\sqrt{2gh}$, where "**g**" is the acceleration due to gravity and "**h**" is the height through which the load is dropped freely. An RCA 931A PMT was placed below the transparent Lucite plate. The PMT was run at 750 V. The output of PMT was connected to the phosphorescent screen oscilloscope (Scientific 300 MHz, SM 340). The ML glow curve can be plotted with the help of SM-340 application software installed on a computer attached to a storage oscilloscope and the ML spectrum was recorded with the help of different band pass interference (400–700 nm) filters [16–18].

Results and discussion

XRD analysis

In order to determine the phase structure, powder XRD analysis has been carried out. XRD patterns of the $SrCaMgSi_2O_7$:Eu^{2+}, Dy^{3+} phosphor are shown in Fig. 2.
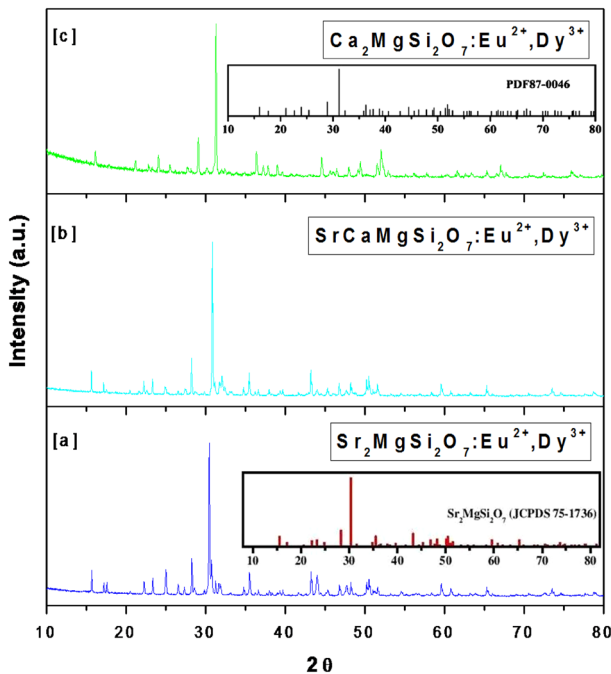

Fig. 2 a–c XRD patterns $Sr_2MgSi_2O_7$:Eu^{2+}, Dy^{3+}; $SrCaMgSi_2O_7$:Eu^{2+}, Dy^{3+} and $Ca_2MgSi_2O_7$:Eu^{2+}, Dy^{3+} phosphors
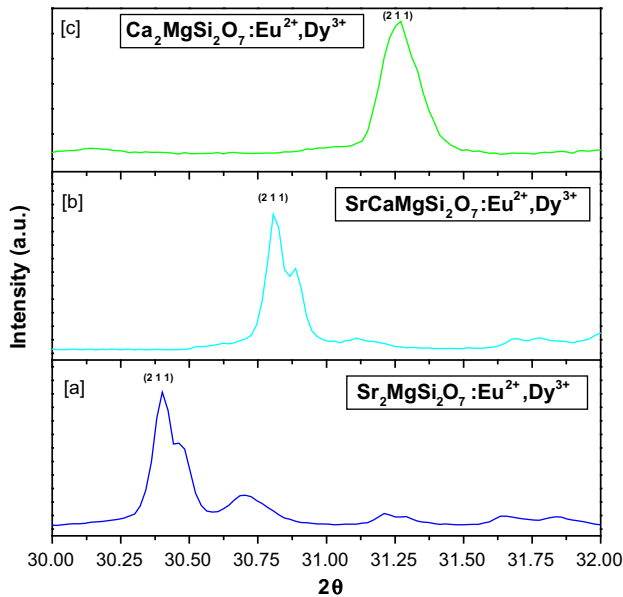
Fig. 3 a–c XRD patterns of $Sr_2MgSi_2O_7$:Eu^{2+}, Dy^{3+}; $SrCaMgSi_2O_7$:Eu^{2+}, Dy^{3+} and $Ca_2MgSi_2O_7$:Eu^{2+}, Dy^{3+} phosphors for the (2 1 1) crystal planes

The standard XRD patterns of $SrCaMgSi_2O_7$ were not found in the International Center for Diffraction Data (ICDD) database but compared with the standard patterns of $Sr_2MgSi_2O_7$ (JCPDS 75-1736) and $Ca_2MgSi_2O_7$ (JCPDS 87-0046) [19, 20] and it could be seen that the major diffraction peaks of $SrCaMgSi_2O_7$:Eu^{2+}, Dy^{3+} are similar for both alkaline earth silicates. The result reveals that the sample $SrCaMgSi_2O_7$:Eu^{2+}, Dy^{3+} has the same crystal structure as $Sr_2MgSi_2O_7$ and $Ca_2MgSi_2O_7$, which indicates that the change of alkaline earth ions induces a small effect on the structure of the sample. The XRD diffraction peaks of $Sr_2MgSi_2O_7$:Eu^{2+}, Dy^{3+}; $SrCaMgSi_2O_7$:Eu^{2+}, Dy^{3+} and $Ca_2MgSi_2O_7$:Eu^{2+}, Dy^{3+} phosphors are shown in Fig. 2a–c.

All the diffraction patterns of the phosphors are quite similar. These results reveal that the phase structure of the $Sr_2MgSi_2O_7$:Eu^{2+}, Dy^{3+}; $SrCaMgSi_2O_7$:Eu^{2+}, Dy^{3+} and $Ca_2MgSi_2O_7$:Eu^{2+}, Dy^{3+} phosphors has an akermanite-type structure, which belongs to the tetragonal crystallography with space group $P\bar{4}2_1m$. This structure was a member of the melilite group and forms a layered compound [21–23]. Other authors also reported this phenomenon. Figure 3a–c shows the peaks of the XRD patterns of $Sr_2MgSi_2O_7$:Eu^{2+}, Dy^{3+}; $SrCaMgSi_2O_7$:Eu^{2+}, Dy^{3+} and $Ca_2MgSi_2O_7$:Eu^{2+}, Dy^{3+} phosphors on the (2 1 1) crystal planes [24].

Transmission electron microscopy (TEM)

The particle size of $SrCaMgSi_2O_7$:Eu^{2+}, Dy^{3+} phosphor is shown in Fig. 4. The TEM study indicates that the particle size of prepared $SrCaMgSi_2O_7$:Eu^{2+}, Dy^{3+}

Fig. 4 TEM images of SrCaMgSi$_2$O$_7$:Eu^{2+}, Dy^{3+} phosphor
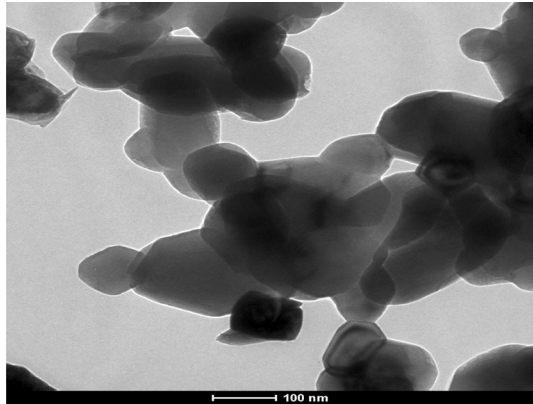
phosphor was in the 80–200 nm range. Moreover, the agglomeration of powder particles was also observed due to the high temperature synthesis.

Field emission scanning electron microscopy (FESEM)

Field emission scanning electron microscopy studies were carried out to obtain information about morphology, grain size, and shape of the synthesized phosphor. The morphologies of prepared SrCaMgSi$_2$O$_7$:Eu^{2+}, Dy^{3+} phosphor were also observed by means of FESEM in Fig. 5a–d with different magnification. The surface morphology of the particles was irregular, which means the distribution of the crystallite sizes is not homogeneous. The morphological images of prepared SrCaMgSi$_2$O$_7$:Eu^{2+}, Dy^{3+} phosphor display that the particles are aggregated tightly with each other due to the high-temperature synthesis method. From the FESEM image, it can be observed that the prepared sample consists of particles with different size distributions. The FESEM results are in good correlation with the TEM studies.

Energy-dispersive X-ray spectroscopy (EDX)

The chemical composition of the powder sample has been measured using EDX. Table 1 shows the compositional element of SrCaMgSi$_2$O$_7$:Eu^{2+}, Dy^{3+} phosphor, which is compared with the standard element. EDX is a standard procedure for identifying and quantifying elemental composition of sample area as small as a few nanometers.

The existence of europium (Eu) and dysprosium (Dy) in prepared SrCaMgSi$_2$O$_7$:Eu^{2+}, Dy^{3+} phosphor is clear in EDX spectra. Their appeared no other emissions apart from strontium (Sr), calcium (Ca), magnesium (Mg), silicon (Si), and oxygen (O) in the EDX spectra of the phosphor. In the EDX spectrum, intense peaks are present, which confirm the formation of SrCaMgSi$_2$O$_7$:Eu^{2+}, Dy^{3+} phosphor in Fig. 6. The elements appear in ratios concomitant with the proportions mixed in the starting materials, which represents the composition of the powder sample.
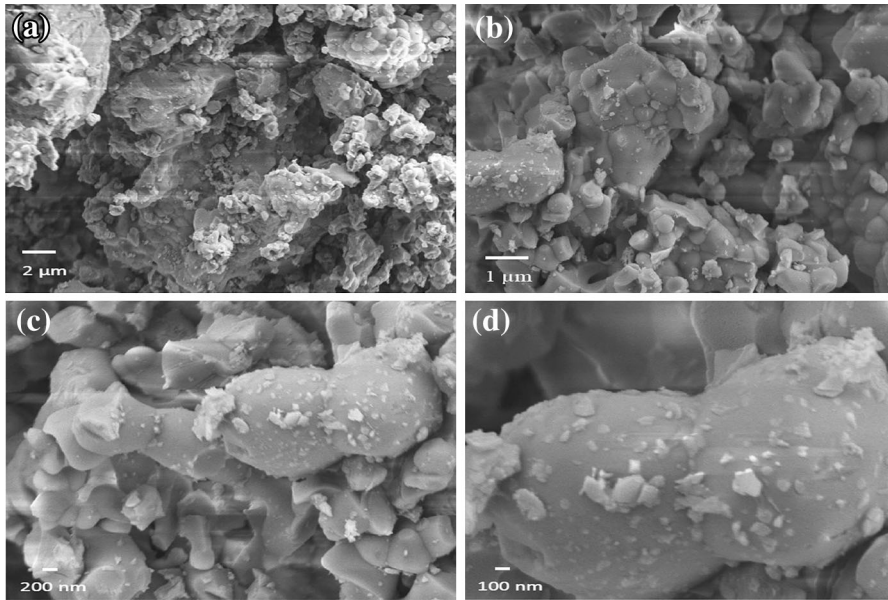
Fig. 5 a–d FESEM image of $SrCaMgSi_2O_7:Eu^{2+}$, Dy^{3+} phosphor

Table 1 Composite element of $SrCaMgSi_2O_7:Eu^{2+}$, Dy^{3+} phosphor

Standard	Elements	Weight (%)	Atomic (%)
SiO_2	O K	29.04	59.73
MgO	Mg K	4.15	5.61
SiO_2	Si K	13.30	15.58
SrF_2	Sr L	22.358	8.62
Wollastonite	Ca L	22.491	8.69
EuF_3	Eu L	0.17	0.04
DyF_3	Dy L	8.49	1.72
Total		100	100

Fourier transform infrared spectra (FTIR)

Figure 7 shows the FTIR spectra of $SrCaMgSi_2O_7:Eu^{2+}$, Dy^{3+} phosphor. FTIR spectra have been widely used for the identification of organic and inorganic compounds. Spectroscopically, the middle infrared region (4,000–400 cm^{-1}) is extremely useful for the study of organic and inorganic compounds. The appearance of the broad band related to the stretching vibrations of O–H groups (3,448.72 cm^{-1}) in the IR spectrum. The hydroxyl (O–H) group in $SrCaMgSi_2O_7:Eu^{2+}$, Dy^{3+} phosphor might be due to presence of moisture through the environment. The free CO_3^{2-} ions have a D3 h symmetry (trigonal planar) and its spectrum is dominated by the band at 1,900–1,700 cm^{-1}. The asymmetric stretching of CO_3^{2-} from carbonates can be observed ~1,967.39, 1,888.93,

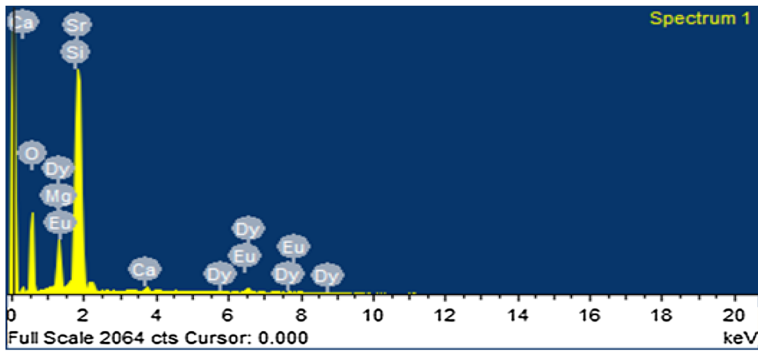**Fig. 6** EDX spectra of SrCaMgSi$_2$O$_7$:Eu^{2+}, Dy^{3+} phosphor

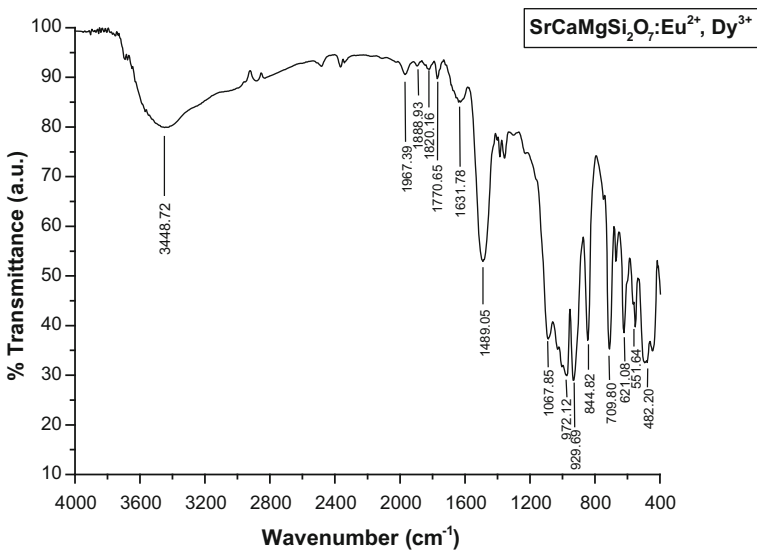**Fig. 7** FTIR Spectra of SrCaMgSi$_2$O$_7$:Eu^{2+}, Dy^{3+}phosphor

1,820.16, and 1,770.65 cm^{-1}. These bands are due to a slight carbonation of the raw materials [SrCO$_3$ and CaCO$_3$]. The vibration band of $\sim$1,631.78 cm^{-1} is assigned due to the Mg^{2+} and bending of the sharp peaks in the region of $\sim$1,489.05 cm^{-1} are assigned due to the bending of Sr^{2+}. The two peaks in the fingerprint region $\sim$844.82 and 709.80 cm^{-1} are assigned due to the Ca^{2+} ions [25, 26].

In the presented spectrum, the absorption bands of silicate groups were clearly evident. According to previous studies on silicate materials, the position of the bands in the 800–1,200 cm^{-1} region can provide information about the number of bridging oxygen atoms bonded to silicon atoms. The stretching modes for the silicate tetrahedral show infrared absorption bands, located at $\sim$1,067.85, 972.12 cm^{-1} was assigned to the Si–O–Si asymmetric stretch, the bands at

~ 929.69 cm^{-1} to the Si–O symmetric stretch. The bands ~ 621.08 and 551.64 cm^{-1} are due to the Si–O–Si vibrational mode. The vibration band around ~ 482.20 cm^{-1} is assigned due to the Mg^{2+}, which is based on the Mg–O modes. The groups [Si$_2$O$_7$] constitute diorthosilicates are the main structural elements of melilites [27, 28].

Photoluminescence (PL)

In order to study the luminescence properties of the prepared SrCaMgSi$_2$O$_7$:Eu^{2+}, Dy^{3+} phosphor, the excitation and emission spectra were recorded and are shown in Fig. 8. An Xe lamp with 360-nm wavelength was used as an excitation source for the measurement. The excitation spectra were observed in the range of 200–425 nm and emission spectra were recorded in the range of 400–650 nm. From the excitation and emission part, flatness is observed due to the instrument limitation. From excitation spectra it is seen that broad bands from 225 to 425 nm (visible light) peaked at 268 and 340 nm. Such a broad excitation band means the prepared SrCaMgSi$_2$O$_7$:Eu^{2+}, Dy^{3+} phosphor can effectively and completely absorb the energy of natural light. For 340-nm excitation, emission spectra were recorded at 490 nm. Under ultraviolet excitation, the broad band is due to transitions of Eu^{2+} between the (4f^7) ground state to the excited state (4f^{6}5d^1) configuration. According to previous research, these emissions (490 nm) correspond to the excited state (4f^{6}5d^1) to ground state (4f^7) configurations of the Eu^{2+} ions and the position of the 5d state of Eu^{2+} is strongly influenced by its surroundings.
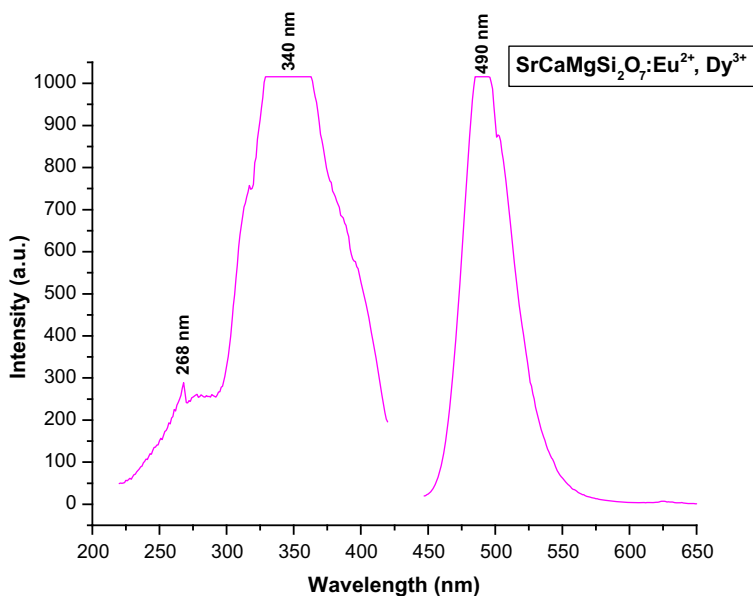

Fig. 8 Excitation and emission spectra of SrCaMgSi$_2$O$_7$:Eu^{2+}, Dy^{3+} phosphor

It is known that the bluish-green emission that peaked at 490 nm corresponds to the transitions of $^4F_{9/2} \rightarrow {}^6H_{13/2,\ 15/2}$ and this emission belongs to hypersensitive transition $J = 2$, which strongly depends on outside environments of Dy^{3+} ions. The Eu^{3+} ion is an activator that provides typical emission at 593 nm (orange) and 615 nm (red), which is not observed in emission spectra, which means Eu^{3+} is successfully converted to the Eu^{2+} ions [24]. However, the special emission peak of Dy^{3+} with the wavelength 486 or 577 nm is also not present, which may be ascribed to the co-doped Dy^{3+} playing a role as a hole-trapped center, which increases the decay time of the phosphor. It is not the cause of the luminescent centers in the host crystal lattice, but the depth of the trap may have an influence on the variation of the lifetimes [29].

Furthermore, the prepared $SrCaMgSi_2O_7:Eu^{2+}$, Dy^{3+} phosphor has an akerman-ite-type structure that belongs to the tetragonal crystallography. According to previous research [24, 30], in akermanite structures the alkaline earth (Sr, Ca, Ba) ions form chains along the c-axis. As the length of the c-axis increases in going from calcium (Ca) to strontium (Sr), the orientation of d orbital will energetically become less favorable in this sequence, which implies that the emission is expected to shift to higher energy (shorter wavelengths). In $Ca_2MgSi_2O_7:Eu^{2+}$, Dy^{3+}, which has the shortest c-axis, the longest wavelength [red shift (low energy)] emission in the series $[Sr_{2-x}Ca_xMgSi_2O_7:Eu^{2+}$, Dy^{3+} $(x = 0, 1, 2)]$ is found. Upon replacing Ca^{2+} by Sr^{2+}, the Eu^{2+} emission shifts to shorter wavelengths in series[blue shift (higher energy)]. From these results, it follows that the influence of the orientation of one d orbital on the emission maximum is large [31]. In our case [$SrCaMgSi_2O_7:Eu^{2+}$, Dy^{3+} phosphor $(x = 1)$], the ratio of Sr/Ca is 1:1. Hence, there is a possibility of the bluish-green emission, which could be explained by the splitting of the $5d$ orbitals and the change in the energy level with different crystal plane spacing.

CIE chromaticity coordinate

In general, the color of any phosphor material is represented by means of color coordinates. The luminescence color of the samples excited under 340 nm has been characterized by the CIE (Commission International de I'Eclairage) 1931 chromaticity diagram. The emission spectrum of the $SrCaMgSi_2O_7:Eu^{2+}$, Dy^{3+} phosphor was converted to the CIE 1931 chromaticity using photoluminescent data and the interactive CIE software (CIE coordinate calculator) diagram as shown in Fig. 9.

Every natural color can be identified by (X, Y) by coordinates that are disposed inside the 'chromatic shoe' representing the saturated colors. Luminescence colors of $SrCaMgSi_2O_7:Eu^{2+}$, Dy^{3+} phosphor are placed in the bluish-green ($X = 0.0952$, $Y = 0.4018$) corners. The chromatic co-ordinates of the luminescence of this phosphor are measured and reached a bluish-green luminescence [17].

Long afterglow (decay)

Figure 10 shows the typical decay curves of $SrCaMgSi_2O_7:Eu^{2+}$, Dy^{3+} phosphor. The initial afterglow intensity of the sintered $SrCaMgSi_2O_7:Eu^{2+}$, Dy^{3+} phosphor
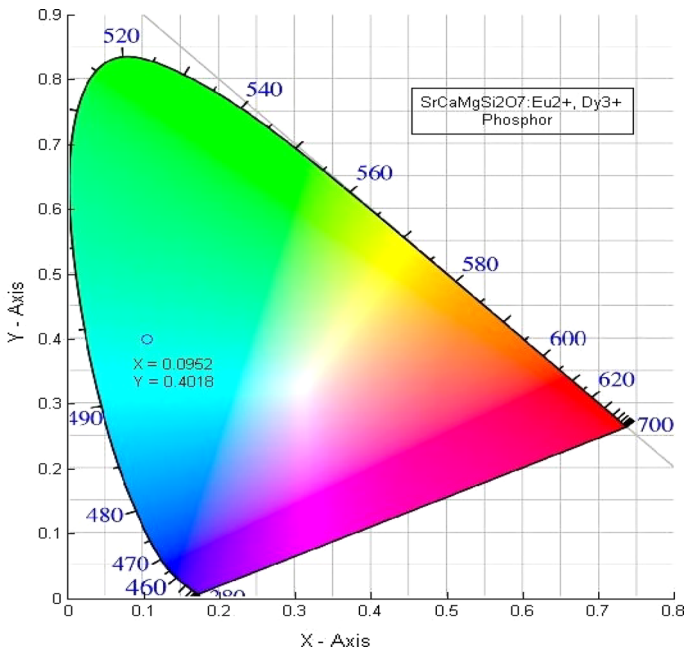
Fig. 9 CIE chromaticity diagram of SrCaMgSi$_2$O$_7$:Eu^{2+}, Dy^{3+} phosphor

was high. The decay times of phosphor can be calculated by a curve-fitting technique and decay curves fitted by the sum of two exponential components have different decay times.

$$I = A_1 \exp\left(-t/\tau_1\right) + A_2 \exp\left(-t/\tau_2\right) \tag{1}$$

where I is phosphorescence intensity, A_1, A_2 are constants, t is time, τ_1 and τ_2 are decay times (in second) for the exponential components. The results indicated that the SrCaMgSi$_2$O$_7$:Eu^{2+}, Dy^{3+} phosphor posses the fast and slow decay process [16–18]. Decay curves are successfully fitted by Eq. (1) and the fitting curve results are shown in Table 2. The results implied that the decay times of SrCaMgSi$_2$O$_7$:Eu^{2+}, Dy^{3+} phosphor consists of two exponential components with different value, and the maximum value reaches 60.33 s.

The co-doped Dy^{3+} acts as trap centers in silicates [32, 33] that trap the electrons generated during the exposure of phosphor to excitation source. The mechanism of afterglow in silicate-based phosphor has been explained by many researchers [34] and may be elaborated as: on receiving exposure to excitation source, an electron of Eu^{2+} (4f^7) is promoted to the 4f^{6}5d^1 band followed by either direct or phonon-assisted escape of the electron from Eu^{2+} to the host conduction band.

The lattice defects close to the bottom of the host conduction band traps the electrons. Huge numbers of electrons are trapped by the traps assisted by Dy^{3+} at various depths [35, 36] making an important role of Dy^{3+} during the long afterglow. After the removal of the excitation source, the electrons excited into conduction
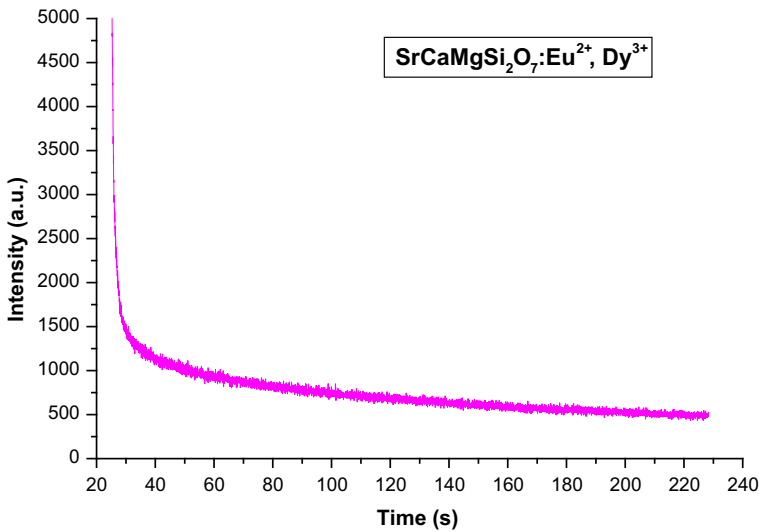
Fig. 10 Decay curves of SrCaMgSi$_2$O$_7$:Eu^{2+}, Dy^{3+} phosphor

Table 2 Fitting results of the decay curves

Phosphor	τ_1 (s)	τ_2 (s)
SrCaMgSi$_2$O$_7$:Eu^{2+}, Dy^{3+}	1.32	60.33

band or excited states of luminescence centers will mostly recombine with holes at the luminescence centres or come back to the ground state of luminescence centres, thus arising static emissions, but still some electrons can be trapped and subsequently stored by electron traps with various depths. The trapped electrons will release with a certain rate at a certain temperature and subsequently recombine at luminescence centres [thermally released to Dy^{3+} ions to form Dy^{2+} or Dy^{3+} + e$^-$]. As a result, we can obtain the long afterglow emission. Thus, the major cause for the afterglow is the number of electrons captured in the traps and its depths from the bottom of the conduction band of host material [37]. Figure 11 shows the mechanism of persistent luminescence in SrCaMgSi$_2$O$_7$:Eu^{2+}, Dy^{3+} phosphor.

The afterglow properties are dominated by the traps, especially for the afterglow duration. If the trap is deep, more energy is needed to release the trapped carriers. Then the duration of the afterglow will be longer since the carriers will be released slowly in the deep trap. However, the trap energy level should not be too deep. Otherwise the afterglow duration may be also shortened because the energy, which needed to release the trap carriers is difficult to obtain at room temperature. Therefore, there should be an optimum trap depth for the generation of the afterglow at room temperature.
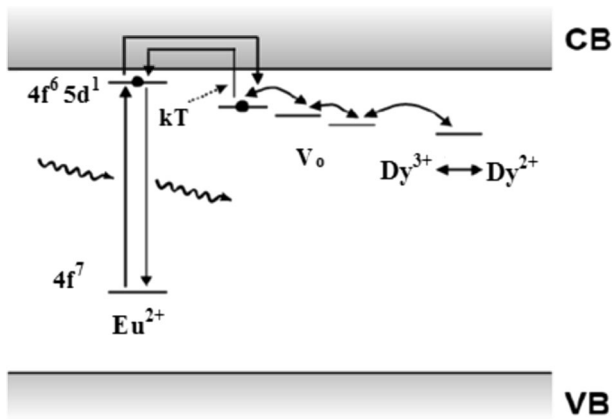
Fig. 11 Mechanism of persistent luminescence in SrCaMgSi$_2$O$_7$:Eu^{2+}, Dy^{3+} phosphor

Mechanoluminecsnce (ML)

Mechanoluminescence (also known as triboluminescence) is an important physical phenomenon where an emission of light is observed due to mechanical deformation of materials, when they are subjected to some mechanical stress like rubbing, cleavage, compressing, impulsive deformation, crushing, grinding, shaking, etc. This phenomenon has been observed in many kinds of solids including ionic crystals, semiconductors, metals, glasses, and organic crystals. In the present ML studies, an impulsive deformation technique has been used. During the deformation of a solid, a great number of physical processes may occur within very short time intervals, which may excite or stimulate the process of photon emission. When a load is applied to the phosphor, initially the ML intensity increases with time, attains a peak value, and then decreases with time. Such a curve between the ML intensity and time of phosphors is known as the ML glow curve [38, 39].

Figure 12a shows that the characteristics curve between ML intensity versus time for different heights (h = 20, 30, 40, 50 cm). The phosphor was fractured via dropping a load [moving piston] of particular mass (400 gm) and cylindrical shape on the SrCaMgSi$_2$O$_7$:Eu^{2+}, Dy^{3+} phosphor. The velocity of the moving piston, holding the impact mass, could be changed by changing the height through which it was dropped. Each time for the ML measurement, the quantity of SrCaMgSi$_2$O$_7$: Eu^{2+}, Dy^{3+} phosphor was kept constant (8 mg). When the moving piston is dropped onto the prepared phosphor at different heights, light is emitted. The photon emission time is nearly 2 ms, when prepared SrCaMgSi$_2$O$_7$:Eu^{2+}, Dy^{3+} phosphor fractures. Two distinct peaks were observed in ML intensity versus time curve. The presence of two peaks indicates that some charge transfer process is involved in ML process. In these ML measurements, maximum ML intensity has been obtained for the 50-cm dropping height and ML intensity increases linearly with the increase of the falling height of the moving piston. The sintered SrCaMgSi$_2$O$_7$:Eu^{2+}, Dy^{3+} phosphor was not irradiated by any excitation source.

Figure 12b shows the time dependence curve of ML intensity of SrCaMgSi$_2$O$_7$:Eu^{2+}, Dy^{3+} phosphor for different impact velocities. It is seen that the ML intensity increases linearly with increasing impact velocity [$\sqrt{2gh}$, (where "**g**" is the acceleration due to gravity and "**h**" is the height through which the load is dropped freely)] of the moving piston. The ML intensity of SrCaMgSi$_2$O$_7$:Eu^{2+}, Dy^{3+} phosphor increases linearly with increasing the mechanical stress.

Figure 13 shows the ML spectrum of SrCaMgSi$_2$O$_7$:Eu^{2+}, Dy^{3+} phosphor. The peak location of the ML spectra (490 nm) and PL (490 nm) are similar, which suggests that the ML spectra also originate from the same emitting center of the Eu^{2+} ions and that the transitions of Eu^{2+} between the excited states (4f^{6}5d^1) to ground state (4f^7) is responsible for the bluish-green ML emission [16, 18].
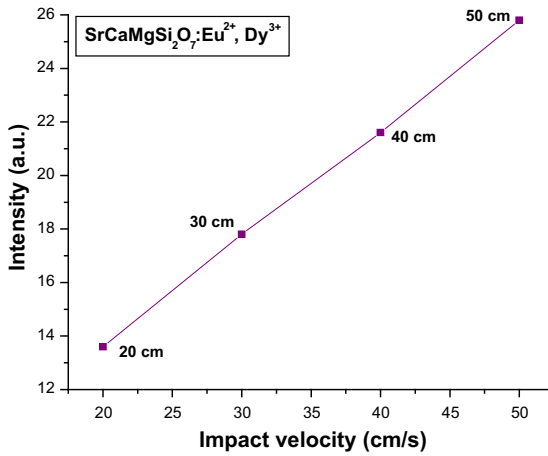
For the ML in SrCaMgSi$_2$O$_7$:Eu^{2+}, Dy^{3+} phosphor, three mechanisms are possible: (1) charged dislocation model, (2) piezoelectrification-induced electroluminescence model, and (3) piezo-electrically induced de-trapping model. The charge dislocation model is not applicable because of these following experimental regions: (1) in elastic region the ML intensity of aluminate and silicate phosphors is repetitive, and (2) intense ML appears when the phosphor is placed inside a transparent illustrating liquid and hydrostatic pressure is applied. As the dislocations cannot move under hydrostatic pressure, the dislocation origin of ML is not possible. In the case of phosphor in nanometer size (1–10 nm), the mean free path of de-trapped electrons is the order of the crystallite size, which is in the nanometer range. For such value of the mean free path, the de-trapped electrons may not get sufficient energy for the impulsive excitation of luminescence centers. In fact, for the SrCaMgSi$_2$O$_7$:Eu^{2+}, Dy^{3+} phosphors of piezoelectrically induced de-trapping model may be applicable.

When a mechanical stress, such as compress, friction, and striking, and so on, was applied on the sintered SrCaMgSi$_2$O$_7$:Eu^{2+}, Dy^{3+} phosphors, a piezo-electric field can be produced. Therefore, in such phosphor, the ML excitation may be caused by the local piezoelectric field near the impurities and defects in the crystals. During the impact on the material, one of its newly created surfaces gets positively charged and the other surface of the crack gets negatively charged. Thus, an intense electric field of the order of 10^6–10^7 Volt cm^{-1} is produced. Under such order of electric field, the ejected electrons from the negatively charged surface may be accelerated and subsequently their impact on the positively charged surfaces may excite the luminescence center [40]. Thus, depending on the prevailing conditions, recombination luminescence may be produced. For the impact velocity v_0, the impact pressure P_0 will be equal to $P_0 = Zv_0$, where Z is a constant. With increasing value v_0 of the trap depth will decrease, therefore, for the trap depth beyond a particular pressure, the traps will be unstable and they will be de-trapped, in which the number of de-trapped electrons will increase with the increasing impact velocity. Thus, the ML intensity will increase proportionally with the increasing value of impact velocity (v_0) [41].

As the impact velocity increases, the impact pressure also increases, leading to an increase in the electric field at local region, which causes a decrease in the trap depth. Hence, the probability of de-trapping increases. From Fig. 12b it can be seen
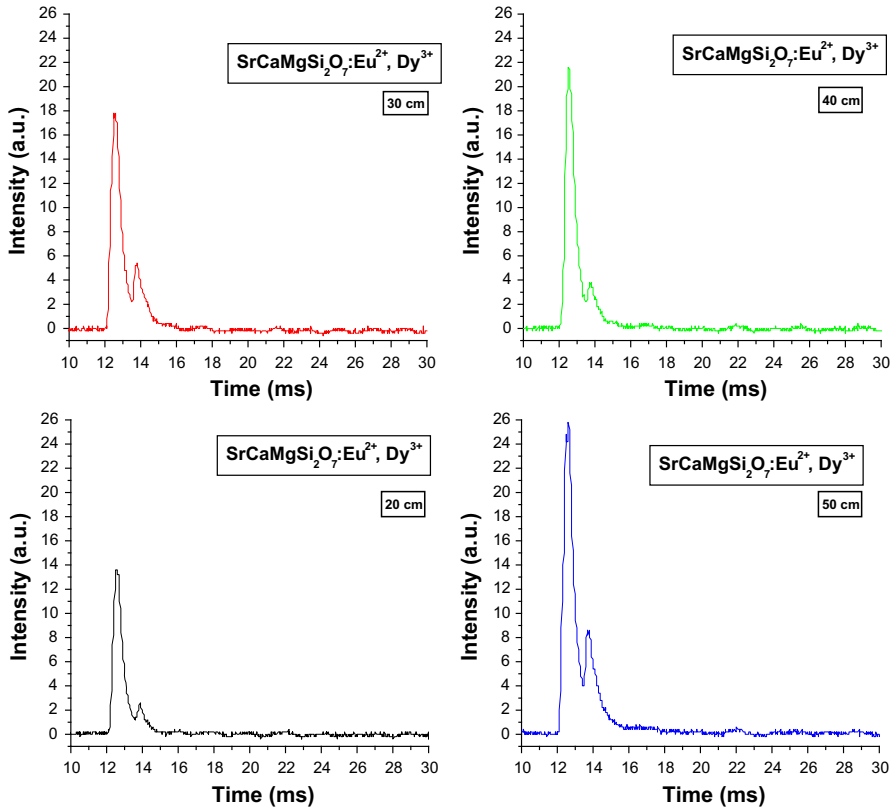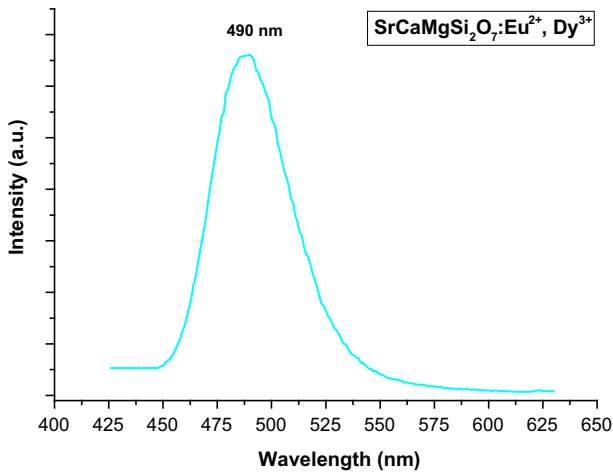
(a)

(b)

Fig. 13 ML spectra of SrCaMgSi$_2$O$_7$:Eu^{2+}, Dy^{3+} phosphor

that with increasing the impact velocity, ML intensity also increases linearly, i.e., the ML intensity of SrCaMgSi$_2$O$_7$:Eu^{2+}, Dy^{3+} phosphors are lineally proportional to the magnitude of the impact velocity, which suggests that this phosphor can be used as a sensor to detect the stress of an object [42, 43].

Conclusions

In summary, SrCaMgSi$_2$O$_7$:Eu^{2+}, Dy^{3+} phosphor was prepared by the traditional high-temperature solid-state reaction method. The tetragonal structure of prepared phosphor was confirmed by XRD analysis. The prepared SrCaMgSi$_2$O$_7$:Eu^{2+}, Dy^{3+} phosphor would emit bluish-green light with a peak at 490 nm that corresponds to the transitions of $^4F_{9/2} \rightarrow {}^6H_{13/2,\ 15/2}$. CIE color chromaticity diagram and ML spectra confirm that the prepared SrCaMgSi$_2$O$_7$:Eu^{2+}, Dy^{3+} phosphor would emit bluish-green color, which indicated that PL is emitted from the same center of Eu^{2+} ions. The phosphorescent life time of SrCaMgSi$_2$O$_7$:Eu^{2+}, Dy^{3+} phosphor can be calculated by a curve-fitting technique, and the decay curves fitted by the sum of two exponential components have different decay times (τ_1 = 1.32 s; τ_2 = 60.33 s) and they possess fast and slow decay processes. It is worthy to note that the dependence between ML intensity of SrCaMgSi$_2$O$_7$:Eu^{2+}, Dy^{3+} and the impact velocity is close to linearity, which suggests that these phosphors can be used as sensors to detect the stress of an object.

References

1. Y. Chen, B. Liu, M. Kirm, Z. Qi, C. Shi, M. True, S. Vielhauer, G. Zimmerer, J. Lumin. **118**, 70–78 (2006)
2. W. Pan, G. Ning, X. Zhang, J. Wang, Y. Lin, J. Ye, J. Lumin. **128**, 1975–1979 (2008)
3. Y. Chen, D. Chen, Ceram. Int. **34**, 2117–2120 (2008)
4. B. Liu, C. Shi, M. Yin, L. Dong, Z. Xiao, J. Alloys Compd. **387**, 65–69 (2005)
5. Z. Xiao, Long afterglow silicate, luminescent materials and its manufacturing method, US Patent No. 6-093-346 (2000)
6. J. Kuang, Y. Liu, J. Zhang, L. Huang, J. Rong, D. Yuan, Solid State Commun. **136**, 6–10 (2005)
7. W. Pan, G. Ning, X. Zhang, J. Wang, Y. Lin, J. Ye, J. Lumin. **128**, 5–9 (2008)
8. B. Lei, Y. Liu, Z. Ye, C. Shi, Chin. Chem. Lett. **15**, 335 (2004)
9. D.R. Vij, *Luminescence of Solids* (Plenum Press, New York, 1998)
10. B.P. Chandra, V.K. Chandra, P. Jha, R. Patel, S.K. Shende, S. Thaker, R.N. Baghel, J. Lumin. **132**, 2012–2022 (2012)
11. X. Wang, C.N. Xu, H. Yamada, K. Nishikubo, X.G. Zheng, Adv. Mater. Weinh. Ger. **17**, 1254 (2005)
12. C.N. Xu, H. Yamada, X. Wang, X.G. Zheng, Appl. Phys. Lett. **84**, 3040 (2004)
13. Y. Liu, C.N. Xu, J. Phys. Chem. B **107**, 3991 (2003)
14. C.N. Xu, X.G. Zheng, T. Wantanabe, M. Akiyama, I. Usui, Thin Solid Films **352**, 273 (1999)
15. H. Zhang, H. Yamada, N. Terasaki, C.N. Xu, J. Electrochem. Soc. **155**, J128 (2008)
16. I.P. Sahu, D.P. Bisen, N. Brahme, R. Sharma, Res. Chem. Intermed. (2014). doi:10.1007/s11164-014-1767-6
17. I.P. Sahu, D.P. Bisen, N. Brahme, Displays **35**, 279–286 (2014)
18. I.P. Sahu, D.P. Bisen, N. Brahme, Lumin. J. Biol. Chem. Lumin. (2014). doi:10.1002/bio.2771
19. JCPDS file number 75-1736, JCPDS International Center for Diffraction Data
20. JCPDS file number 87-0046, JCPDS International Center for Diffraction Data
21. H. Zhang, H. Yamada, N. Terasaki, C.N. Xu, Jpn. J. Appl. Phys. **48**, 04C109 (2009)
22. H. Zhang, H. Yamada, N. Terasaki, C.N. Xu, Electrochem. Solid State Lett. **10**(10), 129–131 (2007)
23. H. Zhang, H. Yamada, N. Terasaki, C.N. Xu, Key Eng. Mater. **388**, 305–308 (2009)
24. H. Wu, Y. Wang, Y. Hu, L. Deng, W. Xie, J. Phys. D Appl. Phys. **42**, 125406 (2009) (7pp)
25. I.P. Sahu, D.P. Bisen, N. Brahme, R.K. Tamrakar, J. Radiat. Res. Appl. Sci. **8**, 104–109 (2015)
26. P. Makreski, G. Jovanovski, B. Kaitner, A. Gajovic, T. Biljan, Vib. Spectrosc. **441**, 62 (2007)
27. I.P. Sahu, D.P. Bisen, N. Brahme, Lumin. J. Biol. Chem. Lumin. (2015). doi:10.1002/bio.2869
28. M.A. Salim, R. Hussain, M.S. Abdullah, S. Abdullah, N.S. Alias, S.A. Ahmad Fuzi, M.N. Md Yusuf, K.M. Mahbor, Solid State Sci. Technol. **17**(2), 59–64 (2009)
29. Y. Lin, Z. Tang, Z. Zhang, X. Wang, J. Zhang, J. Mater. Sci. Lett. **20**, 1505–1506 (2001)
30. S.H.M. Poort, H.M. Reijnhoudt, H.G.T. vander Kuip, G. Blasse, J. Alloys Compd. **241**, 75–81 (1996)
31. L.G. Van Uitert, J. Lumin. **29**, 1–9 (1984)
32. C. Shi, Y. Fu, B. Liu, G. Zhang, Y. Chen, Z. Qi, X. Luo, J. Lumin. **11–13**, 122–123 (2007)
33. T. Aitasalo, J. Holsa, H. Jungner, M. Lastusaari, J. Niittykoski, J. Phys. Chem. B **110**, 4589 (2006)
34. P. Dorenbos, J. Electrochem. Soc. **152**(7), H107 (2005)
35. T. Matsuzawa, Y. Aoki, N. Takeuchi, Y. Murayama, J. Electrochem. Soc. **143**, 2670 (1996)
36. P. Dorenbos, Phys. Status Solidi B **242**, R7 (2005)
37. P. Dorenbos, J. Phys. Condens. Matter **15**, 8417 (2003)
38. B.P. Chandra, J. Lumin. **131**, 1203–1210 (2011)
39. P. Jha, B.P. Chandra, J. Lumin. **143**, 280–287 (2013)
40. B.P. Chandra, R.A. Rathore, Cryst. Res. Technol. **30**, 885 (1995)
41. H. Zhang, H. Yamada, N. Terasaki, C.N. Xu, Thin Solid Films **518**, 610–613 (2009)
42. H. Zhang, H. Yamada, N. Terasaki, C.N. Xu, Int. J. Mod. Phys. B **23**(6 & 7), 1028–1033 (2009)
43. H. Zhang, H. Yamada, N. Terasaki, C.N. Xu, Phys. E **42**, 2872–2875 (2010)